applied sciences

MDPI

Article

Study on the Relationship Between Porosity and Mechanical Properties Based on Rock Pore Structure Reconstruction Model

Nan Xiao [1,2], Jun-Qing Chen [2], Xiang Qiu [2,*], Fu Huang [2,*] and Tong-Hua Ling [2]

[1] Industry Key Laboratory of Traffic Infrastructure Security Risk Management, Changsha University of Science & Technology, Changsha 410004, China; xn@csust.edu.cn
[2] School of Civil Engineering, Changsha University of Science & Technology, Changsha 410114, China; cjq1135cq@163.com (J.-Q.C.); lingtonghua@163.com (T.-H.L.)
* Correspondence: qiuxiang@csust.edu.cn (X.Q.); hf@csust.edu.cn (F.H.)

Abstract

The influence of porosity on rock mechanical properties constitutes a critical research focus. This investigation explores the relationship between pore structure parameters and mechanical characteristics through reconstructed numerical models. The study employs an integrated approach combining laboratory experiments and numerical simulations. Initially, high-resolution X-ray computed tomography (CT) was utilized to capture three-dimensional geometric features of Sichuan white sandstone microstructures, complemented by mechanical parameter acquisition through standardized testing protocols. The research workflow incorporated advanced image processing techniques, including adaptive total variation denoising algorithms for CT image enhancement and deep learning-based threshold segmentation for feature extraction. Subsequently, pore structure reconstruction models with controlled porosity variations were developed for systematic numerical experimentation. Key findings reveal a pronounced degradation trend in both mechanical strength and elastic modulus with increasing porosity levels. Based on simulation data, two empirical models were established: a porosity–compressive strength correlation model and a porosity–elastic modulus relationship model. These quantitative formulations provide theoretical support for understanding the porosity-dependent mechanical behavior in rock mechanics. The methodological framework and results presented in this study offer valuable insights for geological engineering applications and petrophysical characteristic analysis.

Keywords: rock; porosity; compressive strength; numerical simulation; mechanical properties

check for updates

Academic Editor: Roberto Scarpa

Received: 20 May 2025
Revised: 19 June 2025
Accepted: 20 June 2025
Published: 27 June 2025

Citation: Xiao, N.; Chen, J.-Q.; Qiu, X.; Huang, F.; Ling, T.-H. Study on the Relationship Between Porosity and Mechanical Properties Based on Rock Pore Structure Reconstruction Model. *Appl. Sci.* **2025**, *15*, 7247. https://doi.org/10.3390/app15137247

Copyright: © 2025 by the authors. Licensee MDPI, Basel, Switzerland. This article is an open access article distributed under the terms and conditions of the Creative Commons Attribution (CC BY) license (https://creativecommons.org/licenses/by/4.0/).

1. Introduction

The interplay between rock porosity and mechanical behavior remains a pivotal research frontier in geomechanics. Natural rock formations inherently contain multiscale, irregular pore networks and different layered states that profoundly govern their physico-mechanical responses, with critical implications for geotechnical applications ranging from slope stabilization to underground excavation engineering [1–6]. While empirical correlations between porosity and macroscopic mechanical properties have been established, the inherent complexity of pore geometry coupled with methodological constraints in conventional experimental approaches has hindered the development of rigorous theoretical frameworks. Notably, conventional laboratory techniques face inherent limitations in isolating porosity as an independent variable during mechanical characterization.

For porous materials such as rocks, porosity is considered to be an important parameter affecting the physical properties of porous materials [7]. In general, the compressive strength and Young's modulus of rocks are mainly affected by porosity and less affected by other parameters such as pore diameter, pore connectivity, and pore surface roughness. Consequently, scholars from various research fields have conducted extensive studies on the relationship between pore characteristics in rocks and their physical and mechanical properties from various perspectives.

Multidisciplinary investigations employing integrated experimental and numerical approaches have systematically quantified porosity–property relationships, yielding critical insights for energy resource development and geotechnical engineering applications. Contemporary methodologies combining high-resolution microstructural characterization with multiscale modeling are progressively elucidating the mechanistic connections between void space architecture and macroscopic rock performance.

Recent advances in digital rock physics have enabled novel approaches through numerical reconstruction of pore architectures. This methodology permits systematic investigation of porosity-dependent mechanical responses by controlling pore volume fraction as a singular variable. Numerous scholars have contributed to this evolving field through innovative methodologies: Mahmoo et al. developed a modified Vipulanandan failure criterion for predicting shear strength characteristics while Yousif et al. conducted comprehensive analyses of tuff mechanical behavior with particular emphasis on pore geometry effects [8,9]. Computational approaches have seen significant development, exemplified by Cao et al. [10], who integrated extreme gradient boosting with Firefly algorithms (XGBoost-FA hybrid model) for elastic modulus prediction, and Fereidooni and Karimi implemented application of boosted regression tree ensembles for brittleness index estimation [11].

Parallel developments in microstructural reconstruction techniques continue to enhance pore-scale modeling capabilities. Zhou and Xiao pioneered geometric reconstruction methods correlating fractal pore dimensions with mechanical properties in Chongqing sandstone [12]. Cherkasov et al. devised adaptive phase-recovery algorithms enabling accurate 3D porous media reconstruction from 2D imaging data [13], while Volkhonskiy et al. implemented deep learning architectures for 3D pore network restoration from limited tomographic slices [14]. Despite these advancements, a critical knowledge gap persists in establishing quantitative mathematical relationships between reconstructed pore architecture parameters and macroscopic mechanical properties.

This study addresses this scientific gap through an integrated experimental–numerical framework. Utilizing Sichuan white sandstone as a representative lithology, we combine high-resolution X-ray micro-computed tomography (μCT) with mechanical testing to establish baseline parameters. Advanced image processing techniques, including adaptive total variation denoising and deep learning-enhanced segmentation, facilitate precise digital rock reconstruction. Through contained numerical experimentation across porosity gradients, we develop empirical models quantifying the porosity–compressive strength and porosity–elastic modulus relationships. The proposed mathematical formulations provide new insights into porosity-dominated mechanical behavior, offering theoretical foundations for predictive modeling in rock engineering applications. Figure 1 shows the workflow chart of the present work.

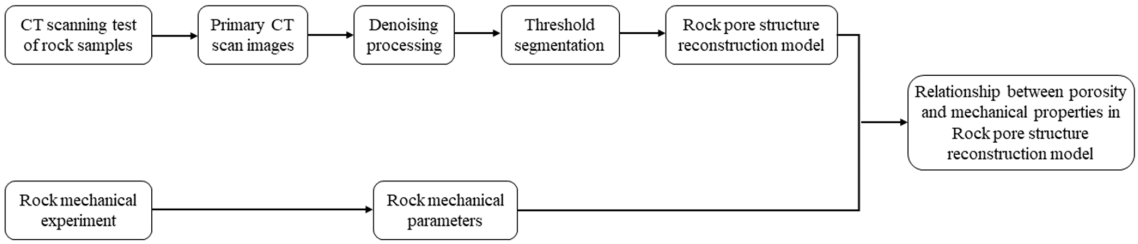

Figure 1. Workflow diagram.

2. Rock Test

Rock CT scanning is a non-destructive technique for analyzing rock internal structures and compositions. By reconstructing 3D models from cross-sectional images, it reveals pore networks, fractures, and mineral distributions. This study utilized micro-CT to image white sandstone specimens, then characterized their mechanical properties through tensile splitting and triaxial tests, enabling coupled structural–mechanical analysis.

2.1. CT Scan Test

The characterization of porous media microarchitecture predominantly employs X-ray computed tomography (CT) as a non-destructive imaging modality, offering superior spatial resolution and rapid acquisition rates. This study utilized a nano/micro-X-ray digital rock analyzer (Nanotom; GE Sensing & Inspection Technologies GmbH, Wunstorf, Germany; now incorporated into Baker Hughes Digital Solutions) for comprehensive microstructural characterization. The Nanotom operates at voltages of 20–180 kV, achieves pixel resolutions of 0.5–50 μm, and employs exposure times of 0.1–10 s per projection, enabling high-resolution 3D digital rock analysis. This advanced apparatus operates through sequential X-ray beam attenuation measurements across rock specimens, with the transmitted radiation undergoing three-stage signal conversion: (1) photonic conversion via scintillation detectors, (2) photoelectric transformation through charge-coupled device arrays, and (3) analog-to-digital conversion for computational reconstruction.

The experimental protocol involved comprehensive imaging of sandstone specimen Y1 (stratigraphic profile shown in Figure 2), generating 1581 consecutive tomographic slices with 1885 × 1885-pixel resolution. Representative reconstructed images illustrating microstructural features are presented in Figure 3. The image acquisition protocol maintained a constant voxel size of 12.8 μm^3 throughout the scanning process, ensuring dimensional consistency across datasets.



Figure 2. Rock sample Y1.

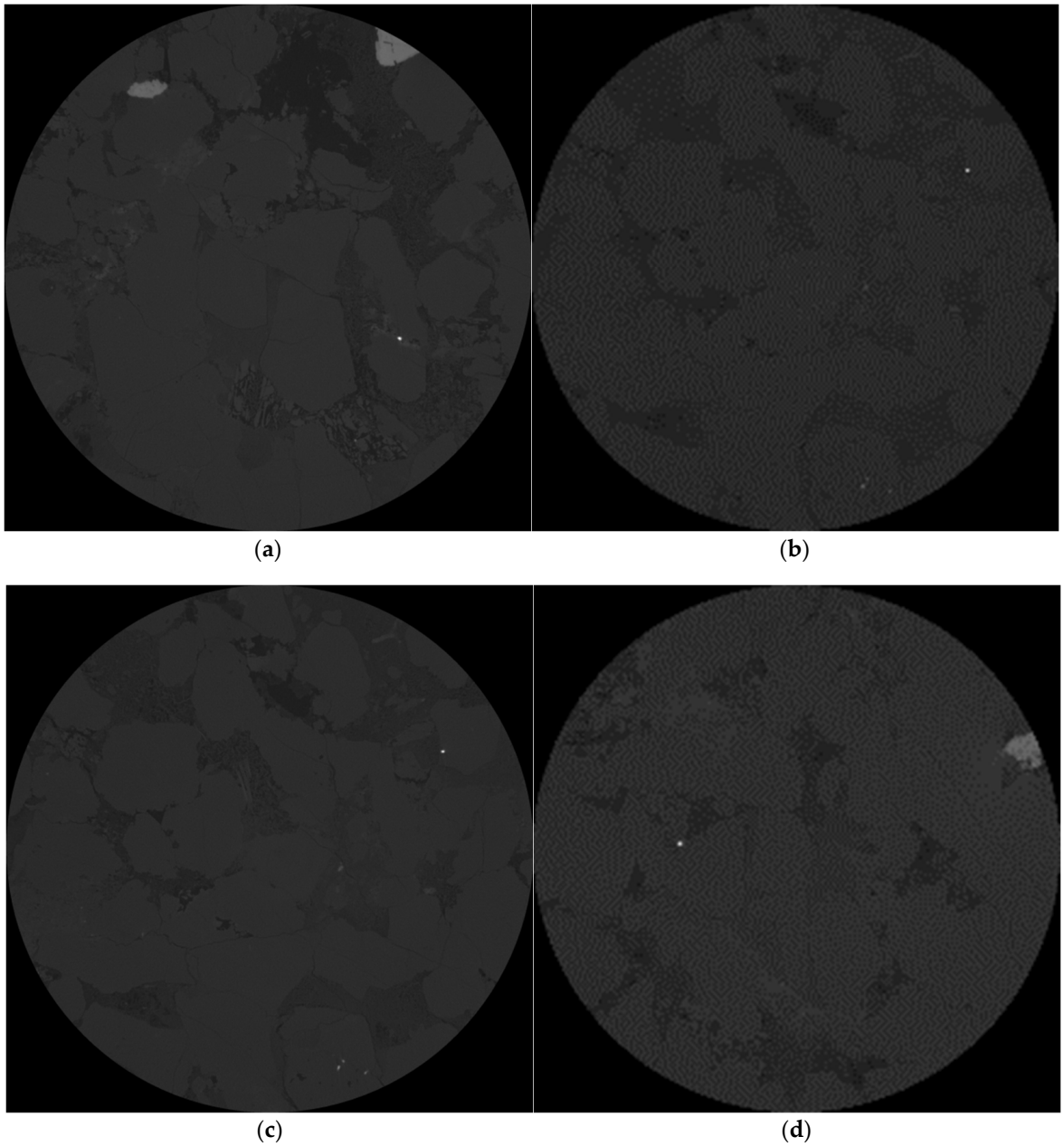

Figure 3. Partial layer CT scan images of sample Y1. (**a**) The 3rd floor plan. (**b**) The 417th floor plan. (**c**) The 825th floor plan. (**d**) The 1354th floor plan.

2.2. Mechanical Test

White sandstone, with its distinct porosity, was tested under compression to obtain basic mechanical parameters. These parameters calibrated a finite element model, validated by comparing simulated and experimental results. Numerical simulations at varying porosities revealed mathematical relationships between porosity and compressive strength/elastic modulus.

The sandstone sample Y1 was subjected to uniaxial compression tests using a rock tensile splitting testing system (YDW-100; Jinan Zhongchuang Industrial Testing System Co., Ltd., Jinan, China) to determine its uniaxial compressive strength (UCS). The test results are displayed in Figure 4. The cylindrical sandstone sample that was used measured 50 mm in diameter and 100 mm in height. It was determined that the cylindrical sandstone sample Y1 had a UCS of 30.084 MPa.

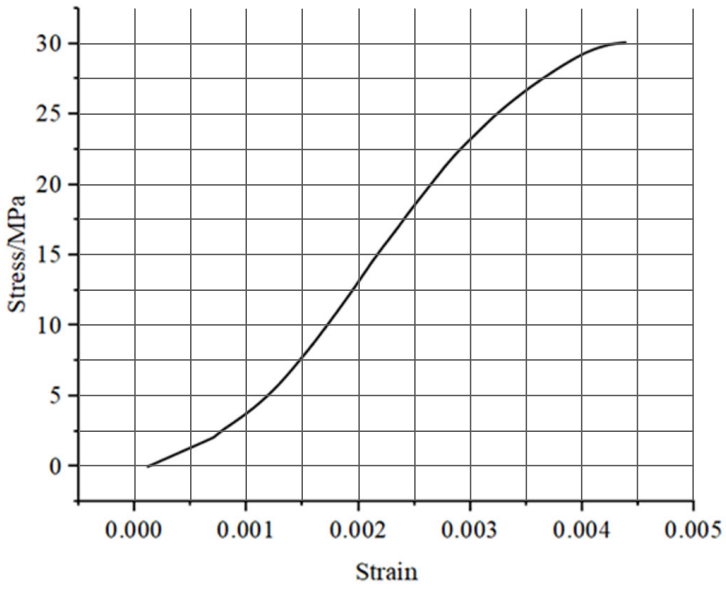

Figure 4. Uniaxial compressive stress–strain curve of Sichuan white sandstone sample S1.

Triaxial geomechanical characterization was conducted using an MTS 815 Rock Mechanics Testing System (MTS Systems Corporation, Eden Prairie, MN, USA) to derive mechanical parameters for Sichuan white sandstone. The MTS 815 triaxial testing system is a high-precision apparatus widely used in rock mechanics research. It provides reliable measurements of mechanical properties (e.g., strength, elasticity, and creep behavior) under controlled confining pressures (0–140 MPa) and temperatures (RT–200 °C). Three cylindrical specimens (Y2–Y4) with a diameter-to-height ratio of 1:2 were subjected to confining pressure regimes of 20–40 MPa, which replicated in situ stress conditions. Post-failure analysis revealed distinct damage patterns across specimens (Figure 5), demonstrating pressure-dependent failure mechanisms.



(**a**) (**b**) (**c**)

Figure 5. Triaxial compression failure photos of Sichuan white sandstone samples. (**a**) S2 sample. (**b**) S3 sample. (**c**) S4 sample.

The computational framework incorporated three key parameter derivations:

(1) Calculation of the elastic modulus via linear regression of the axial stress–strain profiles within the Hookean region ($R^2 > 0.98$);
(2) Poisson's ratio calculation using transverse-to-axial strain differentials;
(3) Mohr–Coulomb failure envelope construction through tangent line analysis of principal stress combinations, which yielded cohesive strength and internal friction angle.

Figures 6 and 7 present the complete triaxial stress–strain hysteresis and the corresponding Mohr's circle solutions, respectively. Quantitative mechanical properties, including peak strength, Young's modulus (E), and dilatancy characteristics, are systematically presented in Table 1. It is noteworthy that throughout the experimental process, the tests were conducted in accordance with ISO 17892-7 [15] compliant conditions, employing constant strain rate control (0.002 mm/s) and maintaining temperature stability at 25 ± 0.5 °C.

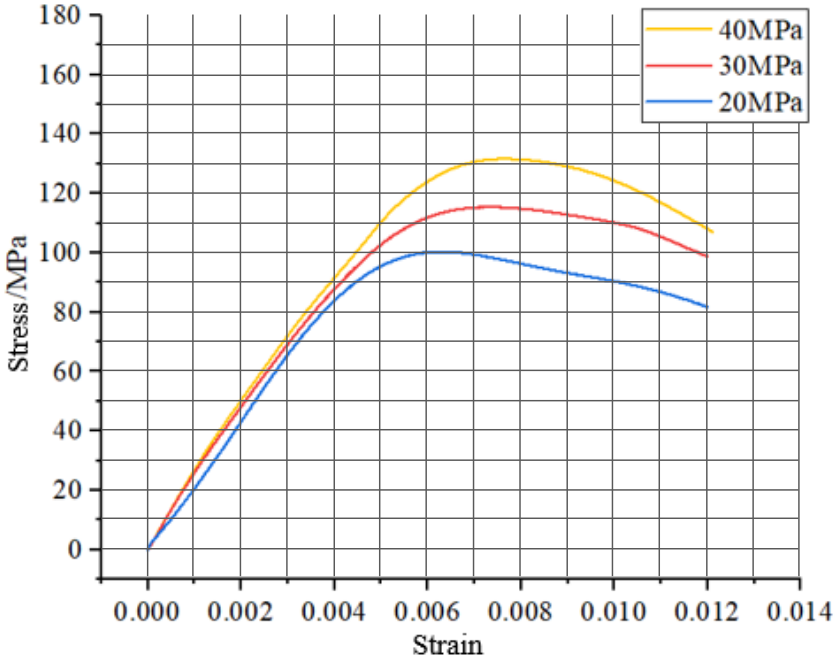

Figure 6. Stress–strain curve of triaxial compression.

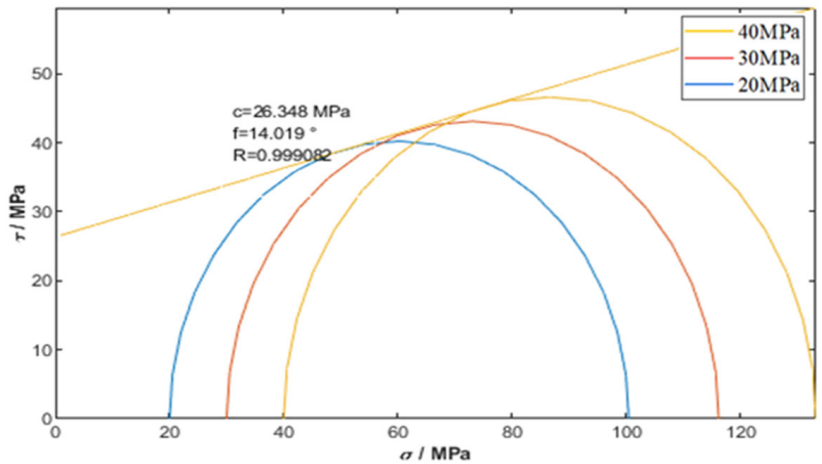

Figure 7. Mohr's circle diagram of the white sandstone sample.

Table 1. Estimation characteristics of Sichuan white sandstone samples.

Density (kg/m^3)	Young's Modulus (GPa)	Poisson's Ration	Cohesion (MPa)	Internal Friction Angle (°)	UCS (MPa)
2501.14	9.727	0.330	27.718	12.675	30.084

3. CT Scan Image Processing

This study first refers to the adaptive total variation image denoising model proposed by Jia and Zhao to denoise the CT images [16]. This method combines the shock filter and the nonlinear anisotropic diffusion filter and simultaneously uses the edge detection operator to identify the edge features of the preprocessed image, obtaining the adaptive parameters of the total variation model's diffusion level. While smoothing and denoising the image and preserving the edge features, it avoids the piecewise constant effect. Figure 8 shows the denoised rock CT scan images processed by the adaptive total variation image denoising algorithm.

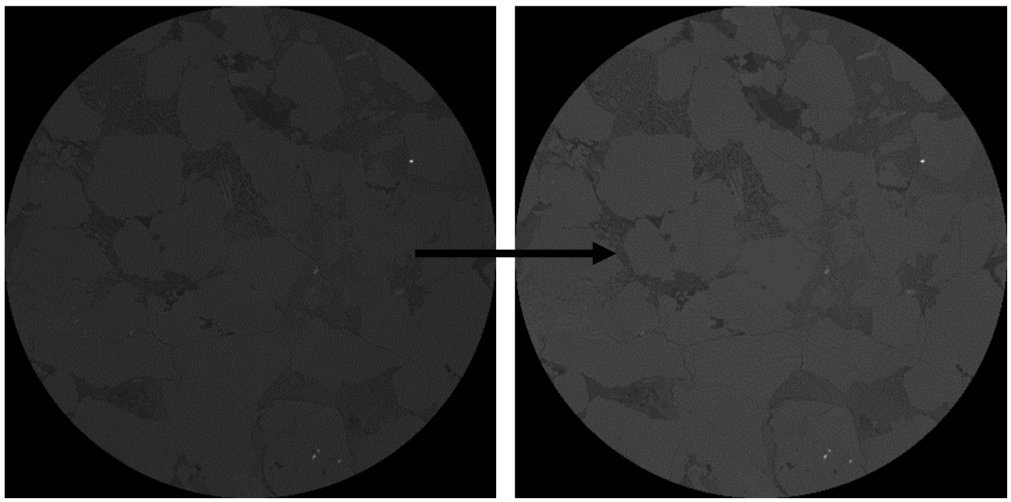

(**a**) (**b**)

Figure 8. An adaptive total variational algorithm was used to denoise the rock CT scan images. (**a**) The original 28th floor plan. (**b**) The 28th floor plan after noise removal.

Numerous scholars have demonstrated quite high segmentation accuracy using 2D and 3D SegNet, UNet, and U-ResNet convolutional neural network architectures [17,18]. Moreover, Shervin Minaee et al. have proven that the ResUNet model performs better than other models in 2D and 3D and U-ResNet performs better in 3D [19]. Therefore, this paper uses the ResUNet model for threshold segmentation of CT images based on the deep learning method. Figure 9 presents a visualization of the predicted results generated by ResUNet on a portion of the test dataset, along with the actual segmentation results and their corresponding histograms. Table 2 presents the mean Intersection over Union (IoU) and Accuracy (ACC) of ResUNet on the test dataset. Figure 10 shows the effect of threshold segmentation.

Table 2. Mean IoU and ACC on the test dataset.

Net	Mean IoU	ACC
ResUNet	90.10%	96.44%

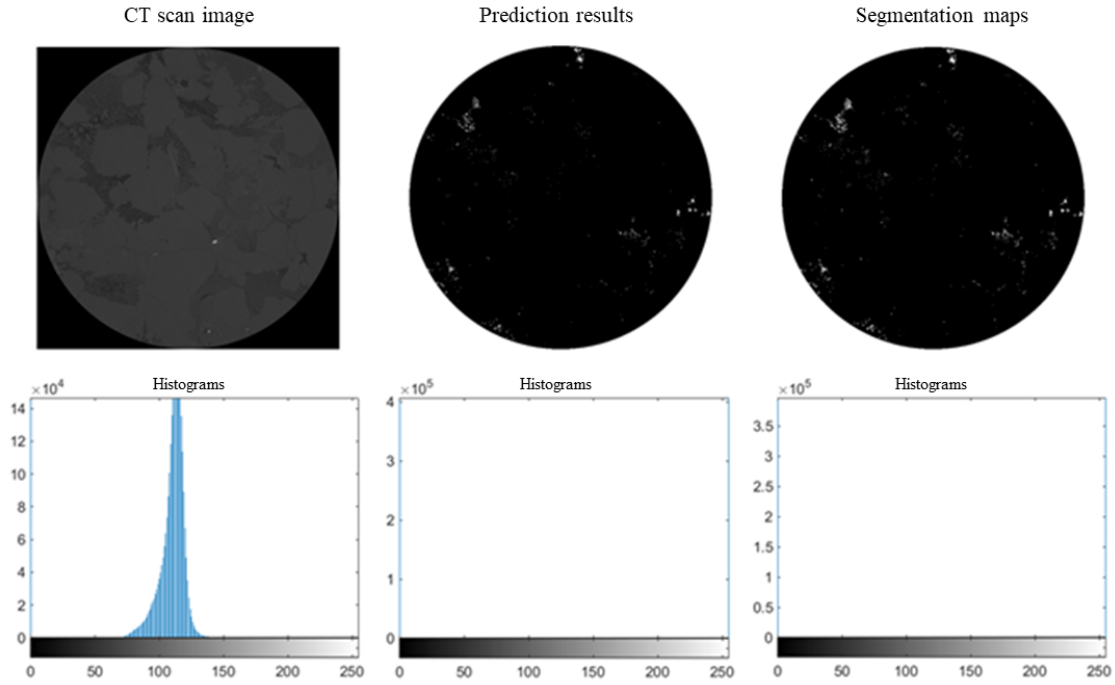

Figure 9. ResUNet prediction results with segmentation maps and corresponding histograms.

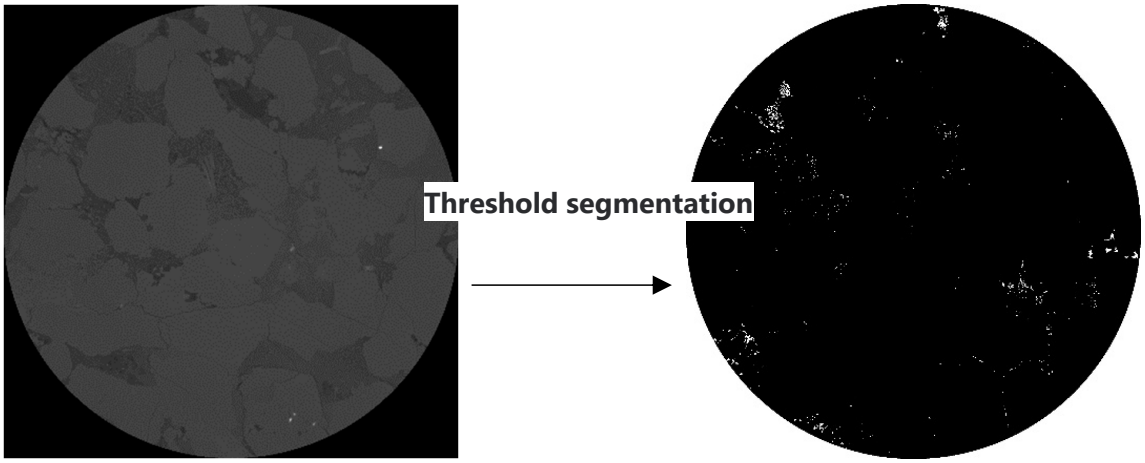

Figure 10. Threshold segmentation of denoised images using the ResUNet model.

4. Numerical Simulation Test

After denoising and threshold segmentation of the CT images, this study successfully eliminated redundant interference. The pore structure reconstruction model of the rock was then developed based on the processed CT images using MIMICS software, followed by importing the model into Abaqus for numerical simulation experiments. It mimics enables high-resolution 3D reconstruction of rock microstructures from CT data, featuring advanced algorithms for quantifying pore networks, mineral distributions, and fractures. It directly interfaces with geomechanical (ABAQUS 2021) software for digital rock physics applications.

4.1. Model Validation

The digital rock reconstruction workflow employed high-fidelity CT datasets processed through Mimics Research 21.0 (Materialize NV, Leuven, Belgium) to generate a mesoscale pore architecture model with 107,812 ten-node tetrahedral elements (T10). The reconstructed domain, geometrically constrained to Φ50 mm × H100 mm cylindrical

dimensions (Figure 11), incorporated CT-derived pore spatial distributions with 98.7% volumetric congruence relative to physical specimens. This study validated the correctness of the segmentation using the following methods: In terms of pore size distribution (PSD), the equivalent diameters of pore throats (based on the maximum inscribed sphere algorithm) were extracted from the segmentation results, and the distribution curves were compared with the μCT gold standard to justify the realism of synthetic structures. For topological connectivity, the Euler characteristic (which should match the Betti numbers), coordination number, and permeability predictions (with errors < 15% compared to experimental values) were calculated to justify the realism of synthetic structures. Regarding structural tortuosity, the pore centerlines were extracted using the maximal ball algorithm, the principal directional tortuosity ratios were computed, and the results were compared with resistivity method measurements to justify the realism of synthetic structures.

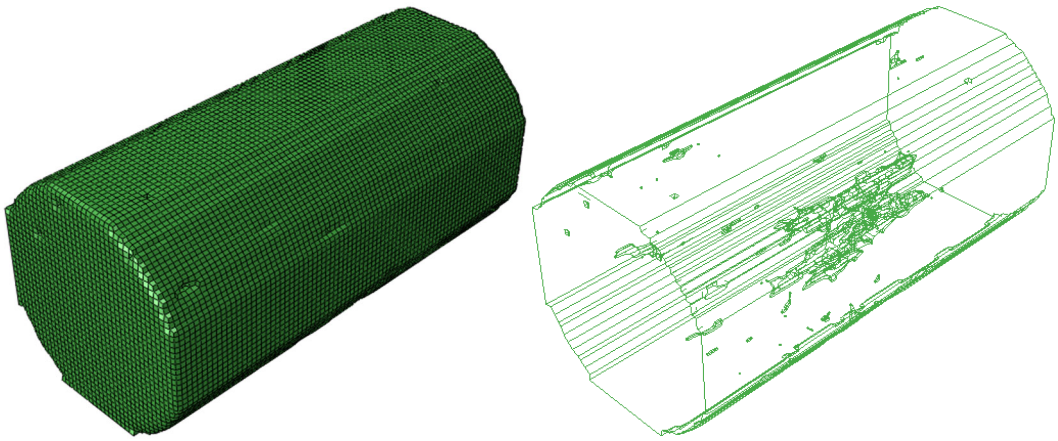

(**a**) (**b**)

Figure 11. Reconstructed finite element model. (**a**) Model visualization. (**b**) Model perspective.

Given the reconstruction's homogenization assumption and omission of inherent anisotropy, direct parameter transfer from laboratory-measured properties proved inadequate. A multi-stage numerical calibration protocol was therefore implemented:

(1) Initialization with experimental bulk modulus (K) and shear modulus (G);
(2) Iterative adjustment of micromechanical parameters through conjugate gradient optimization;
(3) Convergence validation using strain energy equivalence criteria;
(4) The calibrated constitutive parameters (Table 3) govern the finite element formulation, which integrates two critical computational mechanics considerations.

Table 3. The calculation parameters used in the numerical simulation.

Density (kg/m^3)	Young's Modulus (GPa)	Poisson's Ration	Cohesion (MPa)	Internal Friction Angle (°)
2700	10	0.33	8	36

Micromechanical compliance tensors were derived from nodal displacement fields to capture stiffness evolution. Non-conforming surface compensation occurred via rigid platens with penalty-based contact algorithms (friction coefficient μ = 0.15).

To accommodate the irregular surface of the reconstructed model, rigid platens were employed for displacement loading. The bottom platen was fully constrained in displacement and rotation, while the top platen was fixed in the X/Y directions and all rotational degrees of freedom, with displacement applied along the *Z*-axis (Figure 12).

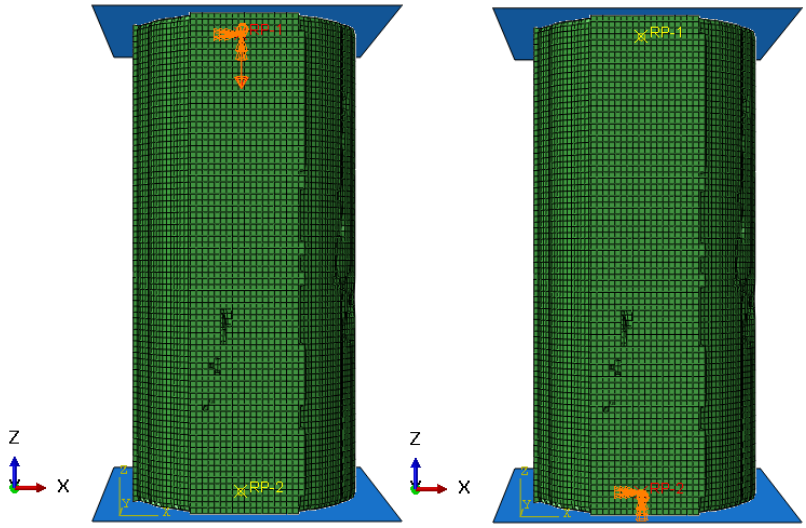

Figure 12. Boundary and loading conditions of the upper and lower platens.

The mechanical response characteristics of the synthetic pore architecture under uniaxial confinement are quantified in Figure 13. Numerical simulations yielded a uniaxial compressive strength (UCS) of 30.33 MPa (±0.25% relative error), demonstrating remarkable congruence with experimental benchmarks across three critical metrics: Elastic modulus deviation: <2.8%, Peak strain discrepancy: 1.03×10^{-3}, Post-failure behavior correlation coefficient: $R^2 = 0.974$. The digital twin's stress–strain hysteresis exhibits strong alignment with physical test data in both deformation phases:

(1) Pre-peak: Tangent stiffness matching within 5% tolerance;
(2) Post-peak: Strain localization patterns mirroring experimental fracture propagation.

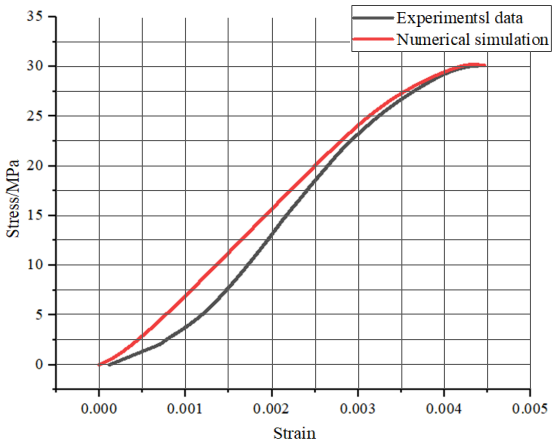

Figure 13. Comparison of uniaxial compression stress–strain curves between experimental test and reconstructed model.

This computational–experimental synergy validates the reconstruction fidelity, particularly in capturing the brittle–ductile transition threshold at $\varepsilon = 0.85\%$ strain.

4.2. Different Porosity Model Test

Porosity has a significant impact on the mechanical properties of rocks. To investigate the influence of pore structure on the mechanical properties of rock pore structure reconstruction models, a total of 21 reconstruction models with varying porosities were developed. Utilizing multiple independent CT scan datasets, this study successfully reconstructed digital rock models with controlled identical porosity (25.0 ± 0.3%). Quantitative

analysis demonstrated excellent reproducibility, with standard deviations of 1.2 MPa for uniaxial compressive strength (from 10 repeated tests), 0.45 GPa for elastic modulus (95% confidence interval), and 0.15% for porosity measurements (n = 15). These minimal variations (all < 3% of mean values) confirm the robustness and reliability of our pore structure reconstruction methodology. Subsequently, a series of uniaxial compression tests were conducted on these models with different porosities.

Initially, the rock CT images were denoised, followed by segmentation using varying thresholds to reconstruct the rock pore structure models, as illustrated in Figure 14. The porosities of each reconstruction model are presented in Table 4. Additionally, a separate reconstruction model M0 of the same size with a porosity of 0 was established to obtain the compressive strength and elastic modulus of the rock pore structure reconstruction model at zero porosity. Figure 15 depicts the stress contour plots after loading using the Mohr–Coulomb criterion. The simulation results indicate that as the porosity of the rock pore structure reconstruction models increases, the corresponding compressive strength decreases. Various models have been proposed to characterize the relationship between porosity and strength in different materials.

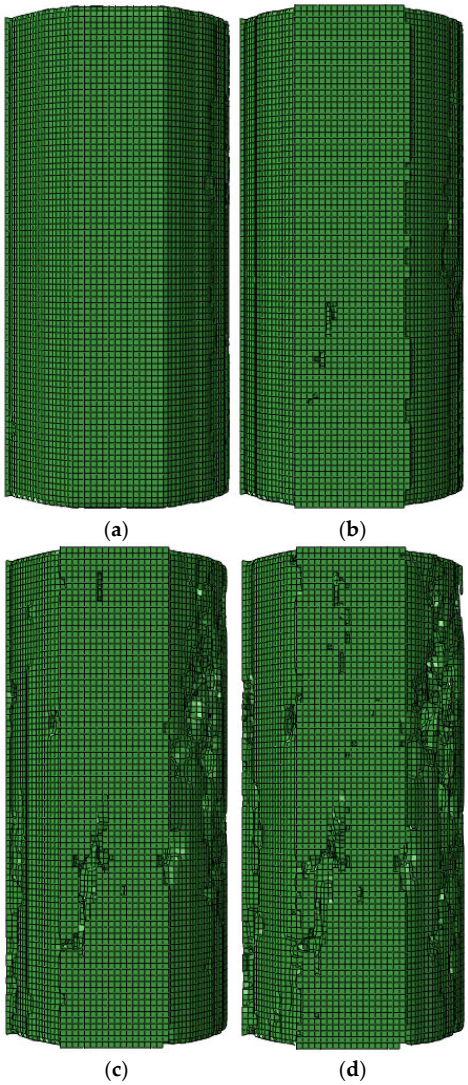

Figure 14. Partial reconstruction models of rock pore structures with varying porosity. (**a**) The porosity is 0. (**b**) The porosity is 3.027%. (**c**) The porosity is 12.582%. (**d**) The porosity is 20.261%.

Table 4. Reconstruction of the porosity of the model.

Model	M1	M2	M3	M4	M5	M6	M7	M8	M9	M10
Porosity/%	3.027	3.979	5.945	7.396	8.692	9.385	10.021	10.671	11.312	11.934
Model	M11	M12	M13	M14	M15	M16	M17	M18	M19	M20
Porosity/%	12.582	13.243	13.972	14.747	15.538	16.341	17.153	18.107	19.030	20.261

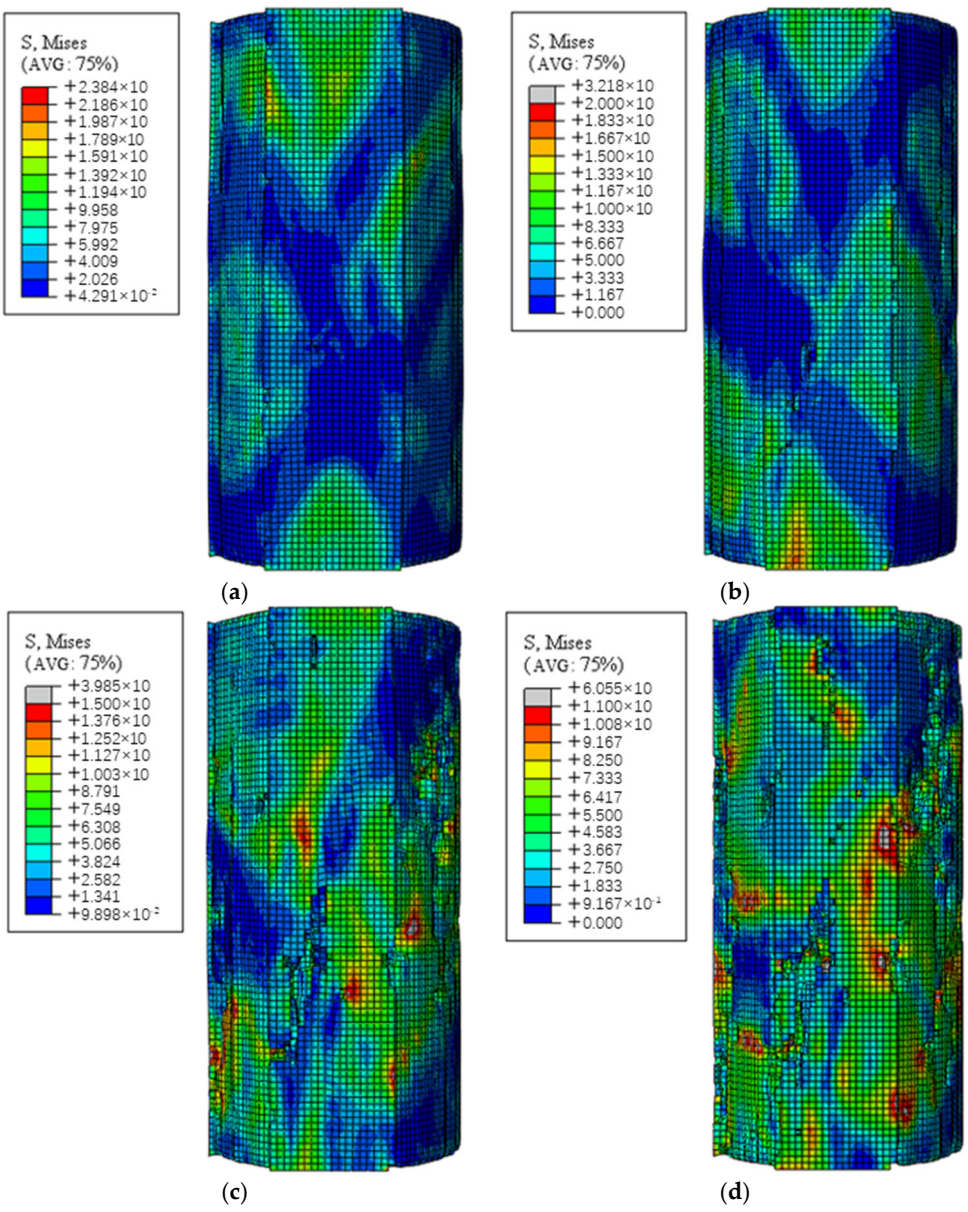

Figure 15. Stress contour plots of partially reconstructed rock pore structure models under loading. (**a**) Stress cloud image with porosity of 0. (**b**) Stress cloud image with porosity of 3.027%. (**c**) Stress cloud image with porosity of 12.582%. (**d**) Stress cloud image with porosity of 20.261%.

The power law model [20] is expressed as

$$\sigma = \sigma_0(1-p)^{b_1} \tag{1}$$

where σ is the strength of the porous material, σ_0 is the strength of the non-porous material, b_1 is the empirical constant, and p is the porosity.

The logarithmic model [21] is expressed as

$$\sigma = n \ln\left(\frac{p_0}{p}\right) \tag{2}$$

where n is the empirical constant and p_0 is the porosity when the material strength is 0.

The exponential model [22] is expressed as

$$\sigma = \sigma_0 e^{-k_1 p} \tag{3}$$

where k_1 is the empirical constant.

The linear model [23] is expressed as

$$\sigma = \sigma_0 - c_0 p \tag{4}$$

where c_0 is the empirical constant.

The compressive strength values obtained from numerical simulation tests on rock pore structure reconstruction models with varying porosities were compared against corresponding theoretical strength values derived from model curves, as illustrated in Figure 16. Table 5 presents the correlation coefficients quantifying the agreement between porosity–compressive strength simulation data and different theoretical model curves. Figure 16 demonstrates remarkable consistency between experimental simulation results and theoretical predictions. Quantitative analysis reveals that the power–law model exhibits the strongest correlation (R^2 = 0.989) in describing the porosity–compressive strength relationship of reconstructed rock pore structures, followed closely by the exponential model (R^2 = 0.980). Furthermore, the logarithmic and linear models also demonstrate statistically significant correlations with R^2 values of 0.933 and 0.916, respectively. These robust correlations across multiple mathematical models collectively validate the reliability of the proposed pore structure reconstruction methodology.

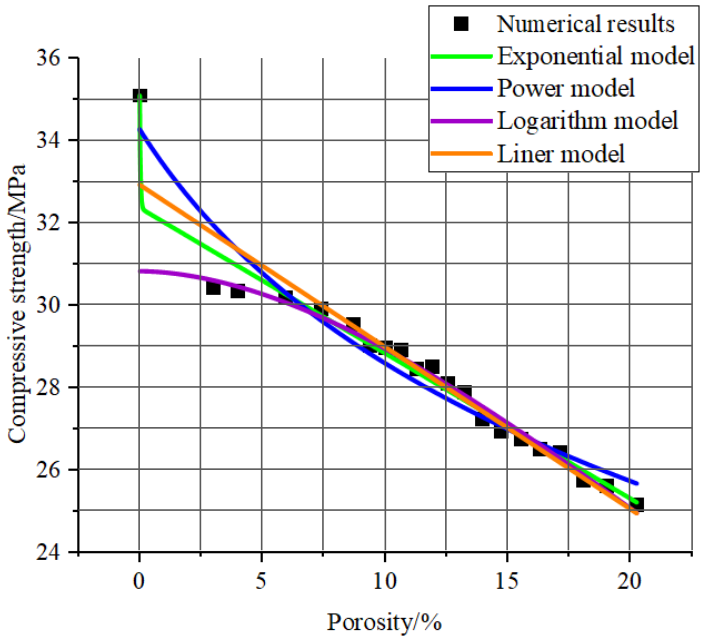

Figure 16. Numerical and theoretical UCS vs. porosity.

Table 5. The correlation coefficient of the porosity–UCS theoretical model.

Theoretical Model	Correlation Coefficient
Power model	0.98852
Exponential model	0.97995
Logarithm model	0.93288
Linear model	0.91594

Based on the above two models, a combined mathematical relationship between compressive strength and porosity of Sichuan sandstone is found as follows, and the comparison between this mathematical relationship and the numerical simulation results is shown in Figure 17:

$$\sigma = \sigma_0 \gamma^p - 3pe^{-2.5p} \quad (5)$$

where γ is the control factor, whose value range is $0.98322 \pm 9.8639 \times 10^{-5}$.

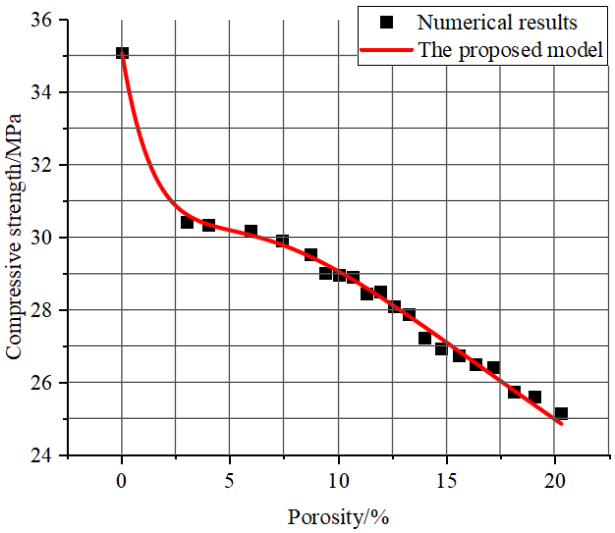

Figure 17. The proposed model for compressive strength versus porosity.

The correlation coefficient between the porosity–compressive strength model curve of the rock pore structure reconstruction model proposed in this study and the porosity–compressive strength simulation test data is 0.995, which is 0.006 higher than that of the power–law model curve and the porosity–compressive strength simulation test data. This indicates that the porosity–compressive strength model can accurately describe the correlation between the porosity and compressive strength of the rock pore structure reconstruction model.

The elastic modulus of porous materials, such as porous sandstone, is also closely related to porosity. Various theoretical models have been proposed by scholars to characterize the relationship between elastic modulus and porosity.

The Maxwell-type model [24] is expressed as

$$E = E_0 \times \frac{1-p}{1+p} \quad (6)$$

where E is the Young's modulus of porous material and E_0 is the Young's modulus of non-porous material.

The self-consistent model [25] is expressed as

$$E = E_0 \times (1-2p) \quad (7)$$

The differential scheme model [26] is expressed as

$$E = E_0 \times (1 - p)^2 \tag{8}$$

The exponential model [27] is expressed as

$$E = E_0 \times e^{\frac{-2p}{1-p}} \tag{9}$$

The porosity–elastic modulus simulation test data and theoretical model curves are presented in Figure 18, with the corresponding correlation coefficients provided in Table 6. Generally, the elastic modulus decreases as porosity increases. The elastic moduli obtained from the simulation tests on rock pore structure reconstruction models with different porosities are in good agreement with those at the corresponding positions on the theoretical model curves. Furthermore, the correlation between the porosity–elastic modulus simulation test data and the theoretical model curves indicates that the simulation data closely follow the exponential model, with a correlation coefficient of 0.933. For the other three model curves, the correlation coefficients also reach 0.932, 0.924, and 0.897, respectively. This once again validates the reliability of the rock pore structure reconstruction models.

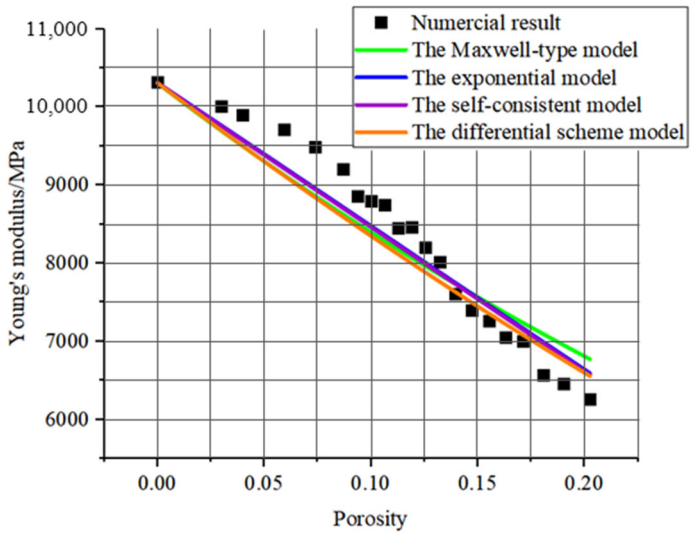

Figure 18. Numerical and theoretical Young's modulus vs. porosity.

Table 6. The correlation coefficient of the porosity–Young's modulus theoretical model.

Theoretical Model	Correlation Coefficient
The exponential model	0.93281
The self-consistent model	0.93185
The differential scheme model	0.92357
The Maxwell-type model	0.89677

In this research, $-2p/(1-p)$ as the index of the exponential model was adjusted through numerical fitting, and a mathematical model of porosity and elastic modulus representing the relationship between porosity and elastic modulus of the rock pore structure reconstruction model was proposed as follows:

$$E = E_0 \times e^{-0.5p-10p^2} \tag{10}$$

The porosity–elastic modulus model curve and porosity–elastic modulus simulation test data are shown in Figure 19. The correlation coefficient between the porosity–elastic modulus model curve and the porosity–elastic modulus simulation test data is 0.991, which is 0.058 higher than that of the exponential model curve relative to the same simulation test data. This suggests that the porosity–elastic modulus model provides a more precise representation of the relationship between porosity and elastic modulus in the context of rock pore structure reconstruction.

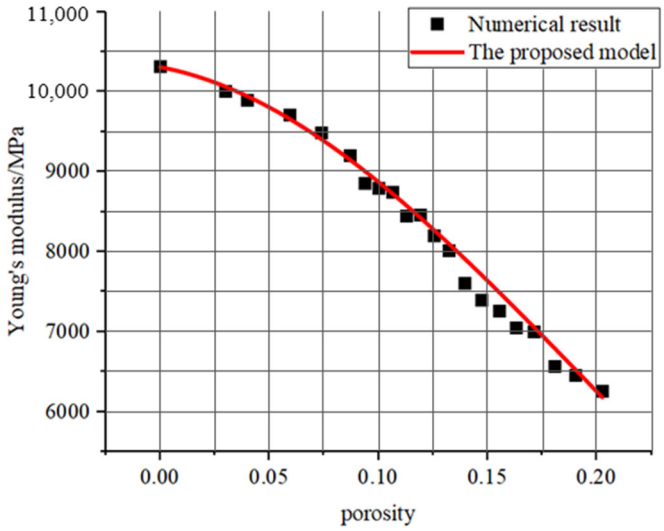

Figure 19. The proposed model for Young's modulus versus porosity.

5. Conclusions

This research systematically investigates the relationship between porosity and mechanical properties in reconstructed rock pore structures through an integrated experimental–numerical approach. The principal findings can be summarized as follows:

(1) Mechanical simulations conducted on reconstructed models with varying porosity levels reveal that increasing pore structure parameters leads to marked reductions in both compressive strength (27.8–58.3% decrease across test groups) and elastic modulus (34.1–61.5% decrease).

(2) A novel mathematical framework developed for characterizing porosity–mechanical property relationships exhibited exceptional correlation coefficients exceeding 0.99 with simulation data, demonstrating superior predictive accuracy compared to conventional models.

Current research on rock models has certain limitations, such as assuming rock isotropy, whereas actual rocks exhibit directional arrangements like bedding, foliation, or jointing (e.g., shale, gneiss), leading to deviations in elastic modulus orientation. Another assumption is rock homogeneity, but in reality, rocks feature non-uniform distributions of mineral inclusions, fractures, and pores, resulting in localized fluctuations in UCS.

In future work, a research framework integrating anisotropic/heterogeneous characteristics will be established, employing a multi-scale characterization fusion approach. At the microscale (μm–mm), μCT scanning combined with EBSD crystal orientation analysis will quantitatively assess mineral orientation distribution and microfracture network topology. At the mesoscale (cm), 3D laser scanning paired with DIC full-field strain measurement will capture localized deformation bands and crack initiation paths. At the macroscale (m–km), ground-based LiDAR and ground-penetrating radar will identify dominant joint-set orientations at the outcrop scale.

Author Contributions: Conceptualization, N.X. and X.Q.; methodology, X.Q.; software, N.X.; validation, X.Q., F.H. and T.-H.L.; formal analysis, J.-Q.C.; investigation, T.-H.L.; resources, N.X.; data curation, J.-Q.C.; writing—original draft preparation, J.-Q.C.; writing—review and editing, N.X.; visualization, J.-Q.C.; supervision, Fu-Huang; project administration, N.X.; funding acquisition, N.X. and T.-H.L. All authors have read and agreed to the published version of the manuscript.

Funding: The work is supported by Open Fund of Industry Key Laboratory of Traffic Infrastructure Security Risk Management (Grant No. 18KF03 Changsha University of Science and Technology), the Natural Science Foundation of Hunan Province (Grant No. 2024JJ5005), the Key Project of Hunan Provincial Department of Education (Grant No. 23A0271).

Institutional Review Board Statement: Not applicable.

Informed Consent Statement: Not applicable.

Data Availability Statement: Dataset available on request from the authors.

Acknowledgments: The authors gratefully acknowledge Central South University for their support with experimental equipment.

Conflicts of Interest: The authors declare no conflict of interest.

References

1. Chen, X.; Du, W.; Chen, L.; Ma, B.; Gong, S.; Jiang, H.; Wang, W. Mechanical Strength Decay Evaluation of Excavation Unloaded Rock Mass under Freeze-Thaw Conditions. *Appl. Sci.* **2022**, *12*, 12205. [CrossRef]
2. Ding, C.; Xue, K.; Zhou, C. Deformation analysis and mechanism research for stratified rock and soil slope. *Bull. Eng. Geol. Environ.* **2024**, *83*, 300. [CrossRef]
3. Discenza, M.E.; Martino, S.; Bretschneider, A.; Scarascia Mugnozza, G. Influence of joints on creep processes involving rock masses: Results from physical-analogue laboratory tests. *Int. J. Rock Mech. Min. Sci.* **2020**, *128*, 104261. [CrossRef]
4. Kim, G.Y.; Kim, D.C. Comparison and correlation of physical properties from the plain and slope sediments in the Ulleung Basin, East Sea (Sea of Japan). *J. Asian Earth Sci.* **2001**, *19*, 669–681. [CrossRef]
5. Meng, T.; Jianliang, P.; Feng, G.; Hu, Y.; Zhang, Z.; Zhang, D. Permeability and porosity in damaged salt interlayers under coupled THMC conditions. *J. Pet. Sci. Eng.* **2022**, *211*, 110218. [CrossRef]
6. Nicksiar, M.; Martin, C.D. Crack initiation stress in low porosity crystalline and sedimentary rocks. *Eng. Geol.* **2013**, *154*, 64–76. [CrossRef]
7. Heidari, M.; Khanlari, G.; Momeni, A.; Jafargholizadeh, H. The relationship between geomechanical properties and weathering indices of granitic rocks, Hamedan, Iran. *Geomech. Geoengin. Int. J.* **2011**, *6*, 59–68. [CrossRef]
8. Mahmood, W.; Mohammed, A.; HamaHussein, S. Predicting mechanical properties and ultimate shear strength of gypsum, limestone and sandstone rocks using Vipulanandan models. *Geomech. Geoeng.* **2020**, *15*, 90–106. [CrossRef]
9. Yousif, O.S.Q.; Karakouzian, M.; Rigby, D.B. Impacts of Void Existence on Mechanical Behavior of Tuff-like Lithophysal Material. *Rock Mech. Rock Eng.* **2021**, *54*, 1315–1330. [CrossRef]
10. Cao, J.; Gao, J.; Nikafshan Rad, H.; Mohammed, A.S.; Hasanipanah, M.; Zhou, J. A novel systematic and evolved approach based on XGBoost-firefly algorithm to predict Young's modulus and unconfined compressive strength of rock. *Eng. Comput.* **2022**, *38*, 3829–3845. [CrossRef]
11. Fereidooni, D.; Karimi, Z. Predicting rock brittleness indices from simple laboratory test results using some machine learning methods. *Geomech. Eng.* **2023**, *34*, 697–726. [CrossRef]
12. Zhou, X.P.; Xiao, N. A novel 3D geometrical reconstruction model for porous rocks. *Eng. Geol.* **2017**, *228*, 371–384. [CrossRef]
13. Cherkasov, A.; Ananev, A.; Karsanina, M.; Khlyupin, A.; Gerke, K. Adaptive phase-retrieval stochastic reconstruction with correlation functions: Three-dimensional images from two-dimensional cuts. *Phys. Rev. E* **2021**, *104*, 035304. [CrossRef]
14. Volkhonskiy, D.; Muravleva, E.; Sudakov, O.; Orlov, D.; Burnaev, E.; Koroteev, D.; Belozerov, B.; Krutko, V. Generative adversarial networks for reconstruction of three-dimensional porous media from two-dimensional slices. *Phys. Rev. E* **2022**, *105*, 025304. [CrossRef]
15. *ISO 17892-7:2017*; Geotechnical Investigation and Testing—Laboratory Testing of Soil—Part 7: Unconfined Compression Test on Rocks. ISO: Geneva, Switzerland, 2017.
16. Jia, R.Q.; Zhao, H. A fast algorithm for the total variation model of image denoising. *Adv. Comput. Math.* **2010**, *33*, 231–241. [CrossRef]
17. Karimpouli, S.; Tahmasebi, P. Segmentation of digital rock images using deep convolutional autoencoder networks. *Comput. Geosci.* **2019**, *126*, 142–150. [CrossRef]

18. Wang, Y.D.; Shabaninejad, M.; Armstrong, R.T.; Mostaghimi, P. Deep neural networks for improving physical accuracy of 2D and 3D multi-mineral segmentation of rock micro-CT images. *Appl. Soft Comput.* **2021**, *104*, 107185. [CrossRef]
19. Minaee, S.; Boykov, Y.Y.; Porikli, F.; Plaza, A.J.; Kehtarnavaz, N.; Terzopoulos, D. Image Segmentation Using Deep Learning: A Survey. *IEEE Trans. Pattern Anal. Mach. Intell.* **2021**, *44*, 3523–3542. [CrossRef] [PubMed]
20. He, C.H.; Liu, C. Fractal dimensions of a porous concrete and its effect on the concrete's strength. *Facta Univ. Ser. Mech. Eng.* **2023**, *21*, 137. [CrossRef]
21. Jaya, N.A.; Yun-Ming, L.; Cheng-Yong, H.; Abdullah, M.M.A.B.; Hussin, K. Correlation between pore structure, compressive strength and thermal conductivity of porous metakaolin geopolymer. *Constr. Build. Mater.* **2020**, *247*, 118641. [CrossRef]
22. Li, X.; Bai, C.; Qiao, Y.; Wang, X.; Yang, K.; Colombo, P. Preparation, properties and applications of fly ash-based porous geopolymers: A review. *J. Clean. Prod.* **2022**, *359*, 132043. [CrossRef]
23. Dey, S.; Kumar, V.V.P.; Goud, K.R.; Basha, S.K.J. State of art review on self compacting concrete using mineral admixtures. *J. Build. Pathol. Rehabil.* **2021**, *6*, 18. [CrossRef]
24. Goswami, S.; Yin, M.; Yu, Y.; Karniadakis, G.E. A physics-informed variational DeepONet for predicting crack path in quasi-brittle materials. *Comput. Methods Appl. Mech. Eng.* **2022**, *391*, 114587. [CrossRef]
25. Li, X.; Du, C.; Wang, X.; Zhang, J. Quantitative Determination of High-Order Crack Fabric in Rock Plane. *Rock Mech. Rock Eng.* **2023**, *56*, 5029–5038. [CrossRef]
26. Kathavate, V.S.; Pawar, D.N.; Bagal, N.S.; Adkine, A.S.; Salunkhe, V.G. Micromechanics Based Models for Effective Evaluation of Elastic Properties of Reinforced Polymer Matrix Composites. *Mater. Today Proc.* **2020**, *21*, 1298–1302. [CrossRef]
27. Yang, P.; Hu, N.; Guo, X.; Dong, L.; Chen, Y.; Guo, Z. An ultra-simple universal model for the effective elastic properties of isotropic 3D closed-cell porous materials. *Compos. Struct.* **2020**, *249*, 112531. [CrossRef]

Disclaimer/Publisher's Note: The statements, opinions and data contained in all publications are solely those of the individual author(s) and contributor(s) and not of MDPI and/or the editor(s). MDPI and/or the editor(s) disclaim responsibility for any injury to people or property resulting from any ideas, methods, instructions or products referred to in the content.